Computers & Fluids 39 (2010) 615–625

Contents lists available at ScienceDirect

Computers & Fluids

journal homepage: www.elsevier.com/locate/compfluid

A front-tracking method for computational modeling of impact and spreading of viscous droplets on solid walls

Metin Muradoglu *, Savas Tasoglu [1]

Department of Mechanical Engineering, Koc University Rumelifeneri Yolu, Sariyer 34450, Istanbul, Turkey

ARTICLE INFO

Article history:
Received 29 May 2009
Received in revised form 14 September 2009
Accepted 28 October 2009
Available online 4 November 2009

Keywords:
Droplet impaction
Contact line
Spreading
Wetting
Multiphase flow
Finite-volume /fronttracking method

ABSTRACT

A finite-difference/front-tracking method is developed for computational modeling of impact and spreading of a viscous droplet on dry solid walls. The contact angle is specified dynamically using the empirical correlation given by Kistler (1993). The numerical method is general and can treat non-wetting, partially wetting and fully wetting cases but the focus here is placed on the partially wetting substrates. Here the method is implemented for axisymmetric problems but it is straightforward to extend it to three dimensional cases. Grid convergence of the method is demonstrated and the validity of the dynamic contact angle method is examined. The method is first tested for the spreading and relaxation of a droplet from the initial spherical shape to its final equilibrium conditions for various values of Eotvos number. Then it is applied to impact and spreading of glycerin droplets on wax and glass substrates and, the results are compared with experimental data of Sikalo et al. (2005). The numerical results are found in a good agreement with the experimental data. Finally the effects of governing non-dimensional numbers on the spreading rate, apparent contact angle and deformation of the droplet are investigated.

1. Introduction

Impact and spreading of a viscous droplet on solid wall is of fundamental importance in many engineering and natural processes including ink-jet printing, spray coating, DNA microarrays, spray cooling and fuel injection in engines [27]. It also finds applications in emerging technologies such as single cell epitaxi [8]. The three-phase moving contact line is a notoriously difficult problem involving highly complicated physical processes and offers a challenge for computational models. During the collision and till the equilibrium, droplet passes various phases in which inertial, viscous, capillary and contact line forces are dominant. It is well known that the no-slip boundary condition yields stress singularity at the contact line since the fluid velocity is finite at the free-surface but zero on the wall [21–23]. This singularity is usually removed by relaxing the no-slip boundary condition with a slip model. Although numerous models and solutions to this problem have been proposed, we are still far from reaching a consensus for a definitive answer [27].

Direct numerical simulation of interfacial flows is a formidable task mainly due to the presence of moving and deforming interface. The existence of the contact line makes the problem even more complicated. A successful numerical modeling of the impact and spreading of a viscous droplet on a partially wetting substrate should address: (i) tracking the interface between the droplet and ambient fluid undergoing extreme deformation in a short time, (ii) accounting for the effects of the interfacial tension, (iii) resolving the contact line singularity and (iv) incorporating the effects of the substrate wettability [12]. Various numerical approaches have been developed to model the impact dynamics of a liquid drop on a solid surface including volume-of-fluid (VOF) method [4,11,16,19,20], level-set method [7,24,28], lattice-Boltzmann method [14], diffuse-interface method [7,12] and immersed boundary method [10]. The common problem in these approaches is the specification of the boundary conditions at the moving contact line. Fukai et al. [11] resolved the contact line singularity by employing a slip model [9]. This method was then extended to include heat transfer and solidification [2,29]. Pasandinideh-Fard et al. [16] employed measured values of dynamic contact angles as a boundary condition in the framework of volume-of-fluid method. Renardy et al. [19] investigated two methods to remove the stress singularity at the moving-contact line. In the first method, the volume-of-fluid function is extrapolated beyond the flow domain. In the second approach, the problem is treated as a three-phase situation mimicking the classical equilibrium conditions at the interface. They found the first method preferable as the second method results in artificial localized flow near the contact line. Later this method was extended to three dimensional flows including solidification by Bussmann et al. [3] and Pasandideh-Fard et al. [17]. Francois and Shyy [10] used an immersed boundary

* Corresponding author. Tel.: +90 212 338 14 73; fax: +90 212 338 15 48.
E-mail address: mmuradoglu@ku.edu.tr (M. Muradoglu).
[1] Present address: Department of Mechanical Engineering, University of California, Berkeley, CA, USA.

0045-7930/$ - see front matter © 2009 Elsevier Ltd. All rights reserved.
doi:10.1016/j.compfluid.2009.10.009

method and treated the contact line boundary condition by setting the contact angle dynamically. In their approach, the contact angle is allowed to vary linearly between the prespecified advancing and receding angles as a function of slip velocity. They compared the results obtained using the static and dynamic contact angles in order to assess the importance and implications of modeling aspect. Spelt [24] took the hysteresis effects into account in specifying the contact angle in the framework of a level-set method but used either constant value of the advancing or receding contact angle based on the sign of the contact line velocity. Once the contact angle is determined, the level-set function is extrapolated to the ghost cells in the solid wall accordingly. A similar approach was also used by Yu et al. [28] again in the framework of a level-set method. Sikalo et al. [20] used a volume-of-fluid method and specified the contact angle dynamically. They imposed the dynamic contact angle indirectly by including a body force on the contact line which was determined from the empirical correlation relating the dynamic contact angle to the capillary number based on the contact line velocity given by Kistler [13]. Mukherjee and Abraham [14] used a lattice-Boltzmann method to study the impact of a viscous droplet on a dry solid substrate and specified the contact angle dynamically again using the Kistler's correlation function. Khatvakar et al. [12] used a diffuse-interface model based on the Cahn-Hilliard theory and studied droplet impact in a wide parameter range. Chen et al. [5] have recently examined two different methods for the treatment of the contact line and found that the stick-slip model (Model-B) is capable of providing parameter independent predictions while the results obtained using the contact line velocity dependent model (Model-A) greatly depend on the prescribed maximum contact line velocity.

In this study, we present a front-tracking method for direct simulations of interfacial flows involving moving contact lines. The front-tracking method developed by Unverdi and Tryggvason [26] has been successfully applied to study a wide range of multiphase flow problems as reviewed by Tryggvason et al. [25]. The front-tracking method has many advantages such as its conceptual simplicity, small numerical diffusion and its ability to incorporate multiphysic effects such as thermocapillarity, electrical field and soluble surfactants [25,15]. In spite of all these advantages, to our knowledge, it has not been applied to the multiphase flow problems involving a moving contact line. In the present method, the contact line is specified dynamically using the empirical correlation given by Kistler [13]. The method is general and can be used to treat non-wetting, partially wetting and fully wetting cases. The method is implemented for axisymmetric problems but it is straightforward to extend it to simulate three dimensional cases. The method is first tested for the spreading and relaxation of a droplet from the initial spherical shape to its final equilibrium conditions for various values of Eotvos number and the results are compared with the analytical solutions in the limiting cases of very small and very large Eotvos numbers. It is then applied to impact and spreading of glycerin droplets on wax and glass substrates and, the results are compared with experimental data of Sikalo et al. [20]. The grid convergence of the method is demonstrated. After validating the computational model against the experimental data, further computations are performed to study effects of governing non-dimensional numbers on the drop spreading.

The paper is organized as follows: The mathematical formulation is briefly described in the next section and the numerical method is presented in Section 3. The results are presented and discussed in Section 4 and some conclusions are drawn in Section 5.

2. Mathematical formulation

The mathematical formulation is briefly described in this section in the context of the finite-difference/front-tracking method for an axisymmetric incompressible flow of Newtonian fluids. Following Unverdi and Tryggvason [26], a single set of governing equations can be written for the entire computational domain provided that the jumps in material properties such as density and viscosity are correctly accounted for and surface tension is included. In an axisymmetric coordinate system, the Navier–Stokes equations are given by

$$\frac{\partial \rho u}{\partial t}+\frac{1}{r}\frac{\partial r\rho u^2}{\partial r}+\frac{\partial \rho u v}{\partial z}=-\frac{\partial p}{\partial r}+\frac{\partial}{\partial r}\left(2\mu\frac{\partial u}{\partial r}\right)+2\mu\frac{\partial}{\partial r}\left(\frac{u}{r}\right)+\frac{\partial}{\partial z}\mu\left(\frac{\partial v}{\partial r}+\frac{\partial u}{\partial z}\right)-\int_A \sigma\kappa\mathbf{n}\delta(\mathbf{x}-\mathbf{x}_f)dA\cdot\mathbf{i}_r$$

$$\frac{\partial \rho v}{\partial t}+\frac{1}{r}\frac{\partial r\rho u v}{\partial r}+\frac{\partial \rho v^2}{\partial z}=-\frac{\partial p}{\partial z}+\frac{1}{r}\frac{\partial}{\partial r}\mu r\left(\frac{\partial v}{\partial r}+\frac{\partial u}{\partial z}\right)+\frac{\partial}{\partial z}\left(2\mu\frac{\partial v}{\partial z}\right)+\Delta\rho g-\int_A \sigma\kappa\mathbf{n}\delta(\mathbf{x}-\mathbf{x}_f)dA\cdot\mathbf{i}_z, \tag{1}$$

where u and v are the velocity components in the radial and axial directions, respectively, p is the pressure, g is the gravitational acceleration, and ρ and μ are the discontinuous density and viscosity fields, respectively. The effects of surface tension is included as a body force in the last term on the right hand side, where σ is the surface tension, κ is twice the mean curvature, and $\mathbf{n}$ is a unit vector normal to the interface, $\mathbf{i}_r$ and $\mathbf{i}_z$ are the radial and axial components of the unit normal vector pointing outward from the drop. The surface tension only acts on the interface as indicated by the delta function, whose arguments $\mathbf{x}$ and $\mathbf{x}_f$ are the point at which the equation is evaluated and the point at the interface, respectively. The Navier–Stokes equations are supplemented by the incompressibility condition,

$$\frac{1}{r}\frac{\partial ru}{\partial r}+\frac{\partial v}{\partial z}=0. \tag{2}$$

We also assume that the material properties remain constant following a fluid particle, i.e., $D\mu/Dt = D\rho/Dt = 0$ where $D/Dt = \frac{\partial}{\partial t}+\mathbf{u}\cdot\nabla$ is the material derivative. The density and viscosity vary discontinuously across the fluid interface and are given by

$$\rho = \rho_d I(r,z,t)+\rho_o(1-I(r,z,t));$$
$$\mu = \mu_d I(r,z,t)+\mu_o(1-I(r,z,t)), \tag{3}$$

where the subscripts d and o denote properties of droplet and the ambient fluid, respectively. $I(r, z, t)$ is the indicator function defined as zero in the bulk fluid and unity in the drop fluid. The indicator function is computed following the procedure described by Tryggvason et al. [25] as follows: The discontinuity is spread onto the Eulerian grid points near the interface resulting in the gradient field

$$\mathbf{G}(\mathbf{x}) = \nabla I = \int_A \mathbf{n}\delta(\mathbf{x}-\mathbf{x}_f)dA, \tag{4}$$

which is zero everywhere except at the interface. Taking the divergence of both sides of Eq. (4) results in

$$\nabla^2 I = \nabla\cdot\mathbf{G}(\mathbf{x}). \tag{5}$$

Eq. (5) is a separable Poisson equation and can be solved efficiently in the vicinity of the droplet.

3. Numerical method

The numerical method is based on the front-tracking/finite-difference method developed by Unverdi and Tryggvason [26]. In this method, a Lagrangian grid is used to track the interface between the droplet and ambient fluid. The Lagrangian grid consists of linked marker points (the front) that move with the local flow velocity interpolated from the stationary Eulerian grid as sketched

in Fig. 1. The piece of the Lagrangian grid between two marker points is called a front element. The Lagrangian grid is used to find the surface tension, which is then distributed onto Eulerian grid points near the interface by using Peskin's cosine distribution function [18], and added to the momentum equations as body forces as described by Tryggvason et al. [25]. At each time step, the indicator function is computed by solving Eq. (5) and is used to set the fluid properties inside and outside the droplet. To do this, unit magnitude jumps are distributed in a conservative manner on the Eulerian grid points near the interface by using Peskin's cosine distribution function [18] and are then integrated to compute the indicator function everywhere. The computation of the indicator function requires solution of a separable Poisson equation (Eq. (5)) and yields a smooth transition of the indicator function across the interface. Then, the fluid properties are set as a function of the indicator function according to Eq. (3). The Lagrangian grid is restructured at every time step by deleting the front elements that are smaller than a prespecified lower limit and by splitting the front elements that are larger than a prespecified upper limit in the same way as described by Tryggvason et al. [25] to keep the front element size nearly uniform and comparable to the Eulerian grid size. Restructuring the Lagrangian grid is crucial since it avoids unresolved wiggles due to small elements and lack of resolution due to large elements. The details of the front-tracking method can be found in the works of Unverdi and Tryggvason [26] and Tryggvason et al. [25].

3.1. Flow solver

The governing equations (Eqs. (1) and (2)) are solved on the stationary staggered uniform Cartesian grid as sketched in Fig. 1. The spatial derivatives are approximated using second order finite-differences and time integration is achieved using a projection method developed by Chorin [6]. The method is briefly described here for completeness. The momentum and mass conservation equations are written in the form

$$\frac{\rho^{n+1}\mathbf{u}^{n+1}-\rho^{n}\mathbf{u}^{n}}{\Delta t}=\mathbf{A}^{n}-\nabla_h p, \tag{6}$$

$$\nabla_h\cdot\mathbf{u}^{n+1}=0, \tag{7}$$

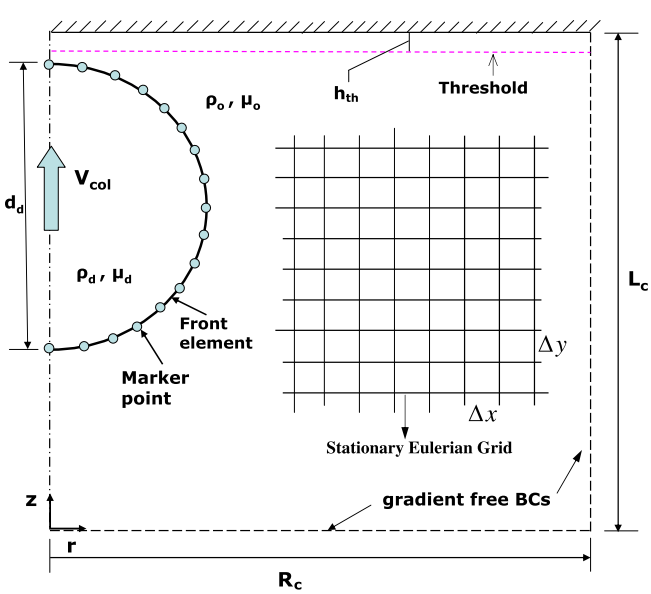

Fig. 1. Schematic illustration of the computational setup. The interface is represented by connected Lagrangian marker points and the flow equations are solved on the stationary uniform Eulerian Cartesian grid. The droplet is initialized near the wall with a spherical shape and uniform collision velocity V_{col}.

where $\mathbf{u}$ is the velocity vector, superscript n denotes the time step, ∇_h is the discrete version of the nabla operator, Δt is the time step. $\mathbf{A}$ represents the advective, diffusive and body force terms in Eq. (1) and is given by

$$\mathbf{A}^{n}=\Big[-\nabla_h\cdot(\rho\mathbf{u}\mathbf{u})+\nabla_h(\mu(\nabla_h\mathbf{u}+\nabla_h^T\mathbf{u}))+\Delta\rho\mathbf{g}-\int_A\sigma\kappa\mathbf{n}\delta(\mathbf{x}-\mathbf{x}_f)dA\Big]^{n}. \tag{8}$$

Eq. (6) is then decomposed as

$$\frac{\rho^{n+1}\mathbf{u}^{*}-\rho^{n}\mathbf{u}^{n}}{\Delta t}=\mathbf{A}^{n}, \tag{9}$$

$$\frac{\rho^{n+1}\mathbf{u}^{n+1}-\rho^{n+1}\mathbf{u}^{*}}{\Delta t}=-\nabla_h p, \tag{10}$$

where $\mathbf{u}^*$ is a provisional (unprojected) velocity ignoring the effect of pressure field. The unprojected velocity field is computed from Eq. (9). Taking the divergence of Eq. (10) and using the incompressibility condition given by Eq. (7), a non-separable Poisson equation is obtained for the pressure field and is given by

$$\nabla_h\cdot\frac{1}{\rho^{n+1}}\nabla_h p=-\frac{1}{\Delta t}\nabla_h\cdot\mathbf{u}^{*}, \tag{11}$$

which is solved on the fixed Eulerian grid using a multigrid method as described by Tryggvason et al. [25]. After obtaining the pressure field from Eq. (11), the velocity field at the new time level is computed as

$$\mathbf{u}^{n+1}=\mathbf{u}^{*}-\frac{\Delta t}{\rho^{n+1}}\nabla_h p. \tag{12}$$

In the present study, we use a first order explicit time integration as described above but second order time accuracy can be easily achieved by a predictor corrector method as described by Tryggvason et al. [25]. Note that the second order scheme is computationally about twice as expensive as the first order scheme and, although not shown here, the first order scheme yields sufficient time accuracy for the problems studied in this paper, i.e., the time stepping error remains smaller than the spatial discretization error.

3.2. Treatment of the contact line

The key ingredient of the present method is the treatment of the boundary conditions at moving contact lines. As mentioned before, the no-slip boundary condition yields stress singularity near the contact line so it requires a special treatment. In the framework of the front-tracking method, the drop interface must be connected to the solid wall explicitly when the droplet gets sufficiently close to the wall since the interface is tracked explicitly by marker points. For this purpose, we assume that the drop interface connects to the wall when the distance between the drop interface and solid wall gets shorter than a prespecified threshold value h_{th} as sketched in Fig. 2. To achieve this, the interface is monitored and the front element crossing the threshold line is detected. Then this element is connected to the solid wall such that the contact angle between the wall and droplet is equal to the apparent contact angle θ_D. In the present method, the apparent contact angle is specified dynamically using Kistler's correlation [13,20] that relates the apparent contact angle to the capillary number defined as $Ca_{cl}=\mu_d V_{cl}/\sigma$ where V_{cl} is the speed of the contact line. Since the Kistler's correlation is valid for small capillary numbers, it is slightly modified here as follows:

$$\theta_{D_i}=f_{\mathrm{Hoff}}(Ca_{clm}+f_{\mathrm{Hoff}}^{-1}(\theta_e)), \tag{13}$$

where f_{Hoff}^{-1} is the inverse function of the *Hoffman*'s function f_{Hoff} defined as

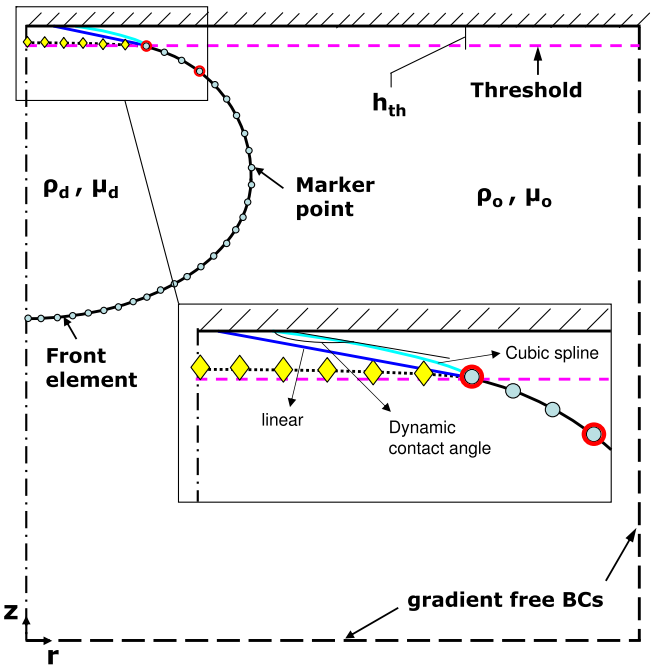

Fig. 2. Schematic illustration of the computational setup for slip contact line method. The droplet is assumed to connect the substrate when it crosses the threshold distance h_{th} using either a linear or cubic extrapolation function as shown in the inset. The contact angle is determined dynamically and imposed explicitly. In the inset, diamonds indicate the marker points to be deleted, dots indicate the marker points and big dots represent the marker points used to fit a cubic spline for predicting the location of the marker point on the substrate.

$$f_{\text{Hoff}}(x) = \arccos\left\{1 - 2\tanh\left[5.16\left(\frac{x}{1+1.31x^{0.99}}\right)^{0.706}\right]\right\}. \tag{14}$$

In Eq. (13), θ_e is the equilibrium (static) contact angle and Ca_{clm} is defined as $Ca_{clm} = \min(Ca_{\max}, Ca_{cl})$ where $Ca_{\max}$ is the cut-off capillary number introduced to avoid too large or too small values of the apparent contact angle. The apparent contact angle is then computed in the advancing and receding phases as

$$\theta_D = \begin{cases} \theta_{D_i} & \text{if } V_{cl} \geqslant 0 \quad \text{(advancing)} \\ 2\theta_e - \theta_{D_i} & \text{if } V_{cl} < 0 \quad \text{(receding)}. \end{cases} \tag{15}$$

The contact line velocity V_{cl} can be specified as the velocity of the marker point on the solid wall. However the velocity of the marker point on the solid wall is found to be too noisy especially when contact line moves slowly, e.g., the droplet approaches static equilibrium conditions. In addition, the dynamic contact angle must be determined iteratively if the velocity of the marker point on the wall is to be used as the contact line velocity since the location and thus the velocity of the marker point on the wall depends on the dynamic contact angle that in turn is determined by the contact line velocity. It is found that such an iteration suffers from lack of convergence as the contact line velocity approaches zero. Therefore the contact line velocity is specified as the velocity of the point where the threshold crosses the droplet interface, which is found to be very robust. Once the apparent contact angle is determined, the front element crossing the threshold line is connected to the solid wall as follows: First the distance between the front element that is to be connected and the wall is predicted assuming that the front element connects to the wall linearly. If this distance is smaller than a prespecified threshold length, l_{th}, then the front element is connected to wall by fitting a cubic curve and imposing the dynamic contact angle as sketched in Fig. 2. Otherwise the front element is connected to the wall using a linear function and again imposing the dynamic contact angle on the wall. The threshold length is typically taken as $l_{th} = 4\Delta x$ where Δx is the Eulerian grid size. Note that we need three points for a cubic fit since one condition is imposed by the apparent contact angle. For this purpose, the first point is selected as the marker point on the front element crossing the interface and the other two are selected such that distance between the selected marker points are approximately equal to the distance between the first marker point and the wall. Typical marker points used in cubic fit are schematically shown in Fig. 2 as big dots. After the front element on the threshold line is connected to the solid wall, the interface is restructured in a similar way as described by Tryggvason et al. [25]. In addition to specifying the contact angle dynamically as explained above, the dynamic contact angle is also used to compute the curvature at the center of the front element adjacent to the solid wall.

3.3. Overall solution procedure

The front-tracking method is coupled with the finite-difference method as follows. In advancing the solutions from time step n to $n+1$, the unprojected velocity field is computed from Eq. (9) and then the front marker points are moved using an explicit Euler method as

$$\mathbf{X}_p^{n+1} = \mathbf{X}_p^n + \Delta t \mathbf{V}_p^n, \tag{16}$$

where $\mathbf{X}_p$ and $\mathbf{V}_p$ are the locations of the marker points and the velocity interpolated from the Eulerian grid onto the location of the marker point $\mathbf{X}_p$ using Peskin's distribution function, respectively. At this stage, the contact line boundary conditions are applied if the drop has passed the threshold line as discussed in the previous section. Then the indicator function is computed based on the new location of the marker points using the procedure described by Tryggvason et al. [25] and the material properties are computed from Eq. (3). After this step, the pressure field is computed from Eq. (11) using the multigrid Poisson solver based on the MUDPACK package [1] and finally the projected velocity field is computed from Eq. (12). The front is restructured at every time step in order to keep the Lagrangian grid nearly uniform by splitting front elements that are larger than a prespecified upper limit and deleting the front elements that are smaller than a prespecified lower limit in the same fashion as described by Tryggvason et al. [25]. As mentioned before, restructuring the front is of crucial importance in order to avoid unresolved wiggles caused by small elements and lack of resolution due to large elements.

4. Results and discussion

4.1. Static test

The method is first tested for relaxation of a viscous droplet from a spherical initial conditions to its final equilibrium shape. For this test, a spherical droplet of radius R_o is initialized near the solid surface as shown in the inset of Fig. 3 and is allowed to spread until its final static shape is reached for various values of the Eotvos number ($Eo = (\rho_d - \rho_o)gR_o^2/\sigma$) that represents the ratio of gravitational force and surface tension force. Note that this test case was recently used by Chen et al. [5]. The static shape of the droplet generally depends on the equilibrium contact angle θ_e and the Eotvos number. In the limit of vanishing Eotvos numbers, i.e., $Eo \ll 1$, the equilibrium shape of the droplet is determined by the surface tension force and takes a shape of spherical cap with the maximum height of the droplet, H_o, given by

$$H_o = R_o(1 - \cos\theta_e)\left(\frac{4}{2 + \cos^3\theta_e - 3\cos\theta_e}\right)^{1/3}. \tag{17}$$

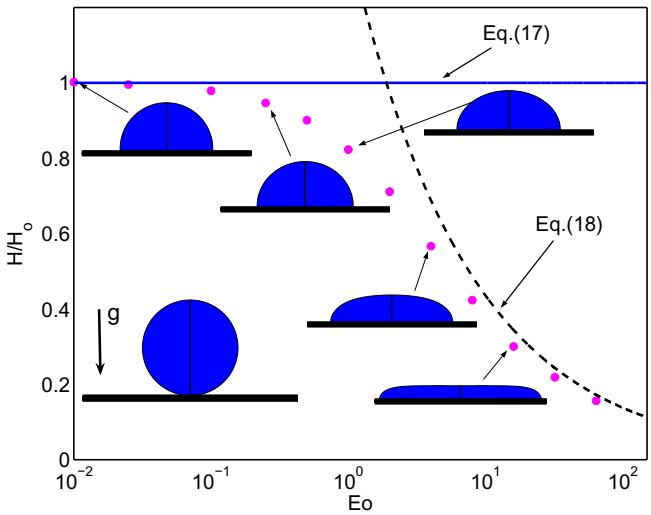

Fig. 3. The normalized static droplet height versus Eotvos number in the range $Eo = 0.01$ and $Eo = 64$. Solid and dashed lines denote the analytical solutions for the limiting cases of $Eo \ll 1$ and $Eo \gg 1$, respectively. The inset shows the initial conditions for the droplet relaxation test.

On the other hand, when $Eo \gg 1$, the shape of the droplet is controlled mainly by the competition between the gravitational and surface tension forces and, the maximum height of the droplet is proportional to the capillary length [5], i.e.,

$$H_\infty = \frac{2H_o \cos(\theta_e/2)}{\sqrt{Eo}}, \tag{18}$$

where H_o is given by Eq. (17). Computations are performed for this test case and the results are compared with the asymptotic solutions given by Eqs. (17) and (18). For this purpose, the equilibrium contact angle is set to $\theta_e = 93^\circ$ and the dynamic angle is used at the contact line. Focus here is placed on the static shape of the droplet. The computational domain extends five drop radii both in the axial and radial directions, and is resolved by a 256×256 uniform Cartesian grid. Fig. 3 shows the normalized steady-state droplet height as a function of Eotvos number together with the steady shapes of droplet in the range of $Eo = 0.01$ and 64. This figure clearly shows that the computed normalized droplet height agrees well with the asymptotic solutions given by Eqs. (17) and (18) for $Eo \ll 1$ and $Eo \gg 1$, respectively. For the intermediate values of Eotvos number, the transition between a spherical cap and a puddle shape occurs.

4.2. Comparison with the experimental data

The numerical method is then applied to impact and spreading of a glycerin droplet and the results are compared with the experimental data of Sikalo et al. [20]. The cases studied experimentally by Sikalo et al. [20] and computationally here are summarized in Table 1. The computational domain extends 5 drop radii both in the radial and axial directions. A uniform Cartesian grid is used in all the results presented in this paper. The droplet is initially spherical and is placed near the wall with a uniform impact velocity, V_{col}, as shown in Fig. 1. The surrounding air is initially quiescent. The viscosity and density ratios are set to $\rho_d/\rho_o = \mu_d/\mu_o = 20$ in all the results presented here. Note that the density and viscosity ratios are an order of magnitude larger in the experiments than those specified here. However, although not shown here, it is found that a further increase in the property ratios does not affect the computational results significantly. Therefore the property ratios are kept small in order to avoid numerical instability and to reduce the computational time. Physical quantities are non-dimensionalized using the initial drop diameter as length scale and d_d/V_{col} as the time scale. First the evolution of droplets after impacting the solid surface is shown in Figs. 4 and 5 for the Cases 1 and 2 in Table 1, respectively. A 512×512 grid resolution is used in the simulations. As will be discussed below, this grid resolution is sufficient for the grid convergence. The static contact angle is set to $\theta_e = 93^\circ$. Note that static contact angles are reported by Sikalo et al. [20] as 90° and 97° for advancing and receding contact angles, respectively. Here we use a fixed value both for the advancing and receding contact angles in order to avoid oscillations in the dynamic contact angle as droplet approaches the final equilibrium conditions. In Figs. 4 and 5, the velocity vectors and pressure contours are plotted near the droplet interface in order to demonstrate the overall quality of computational results. It is seen that the interfaces are smooth and there is no artificial localized flow near the contact lines in both cases, which may qualitatively indicate the overall performance of the present method. The performance of the method is then quantified by comparing the computational results with the experimental data for the Cases 1–3, i.e., glycerin droplet impacting and spreading on a wax. The experimental and computational spread factors are plotted in Fig. 6a as a function of non-dimensional time. The spread factor is defined as the radius of the wetted spot normalized by the equivalent drop radius. This figure shows that the spread factor is well predicted and the maximum difference between the experimental and computational spread factors is below 7%. The time evolution of the contact angle is plotted in Fig. 6b for the same cases. The contact angle is calculated as an average of the contact angles computed at the centers of the front elements that lie in the threshold (see, Fig. 2) by simply fitting a cubic spline to the marker points of the front element and its immediate neighbors. The computational results are in a reasonable agreement with the experimental results for all three cases. There is an approximately 20° disagreement between computational and experimental values just before reaching the equilibrium contact angle. This can be partly explained by the fact that it is not clear exactly where the contact angle is measured in the experiments and there is about ±5% measurement error in the experimental data [20]. Note that the contact angle varies significantly from one element to its neighbors especially near the solid wall. We emphasize here that the computed contact angle correctly relaxes to the equilibrium contact angle in all the cases presented in this paper as the droplet approaches to final static conditions. The computations are repeated for the Case 1 using static and dynamic contact angle models for a longer period of time in order to show the performance of the present method in the receding phase. The computations are performed using a relatively coarser (384×384) grid in order to facilitate the long time simulation. The results are plotted in Fig. 7 and compared with the volume-of-fluid (VOF) simulation as well as the experimental data of Sikalo et al. [20]. As can be seen in this figure, the present method underpredicts the spreading rate while the VOF model overpredicts. In addition, the dynamic contact angle model performs better than the static contact angle model in the receding phase but there is no significant difference in the

Table 1
List of cases studied experimentally by Sikalo et al. [20] and computationally here.

Cases	Liquid	Wall	Impact velocity	*We*	*Re* (m/s)	θ_e (°)
1	Glycerin	Wax	4.1	802	106	93
2	Glycerin	Wax	1.41	93	36	93
3	Glycerin	Wax	1.04	51	27	93
4	Glycerin	Glass	4.1	802	106	15
5	Glycerin	Glass	1.41	93	36	15
6	Glycerin	Glass	1.04	51	27	15

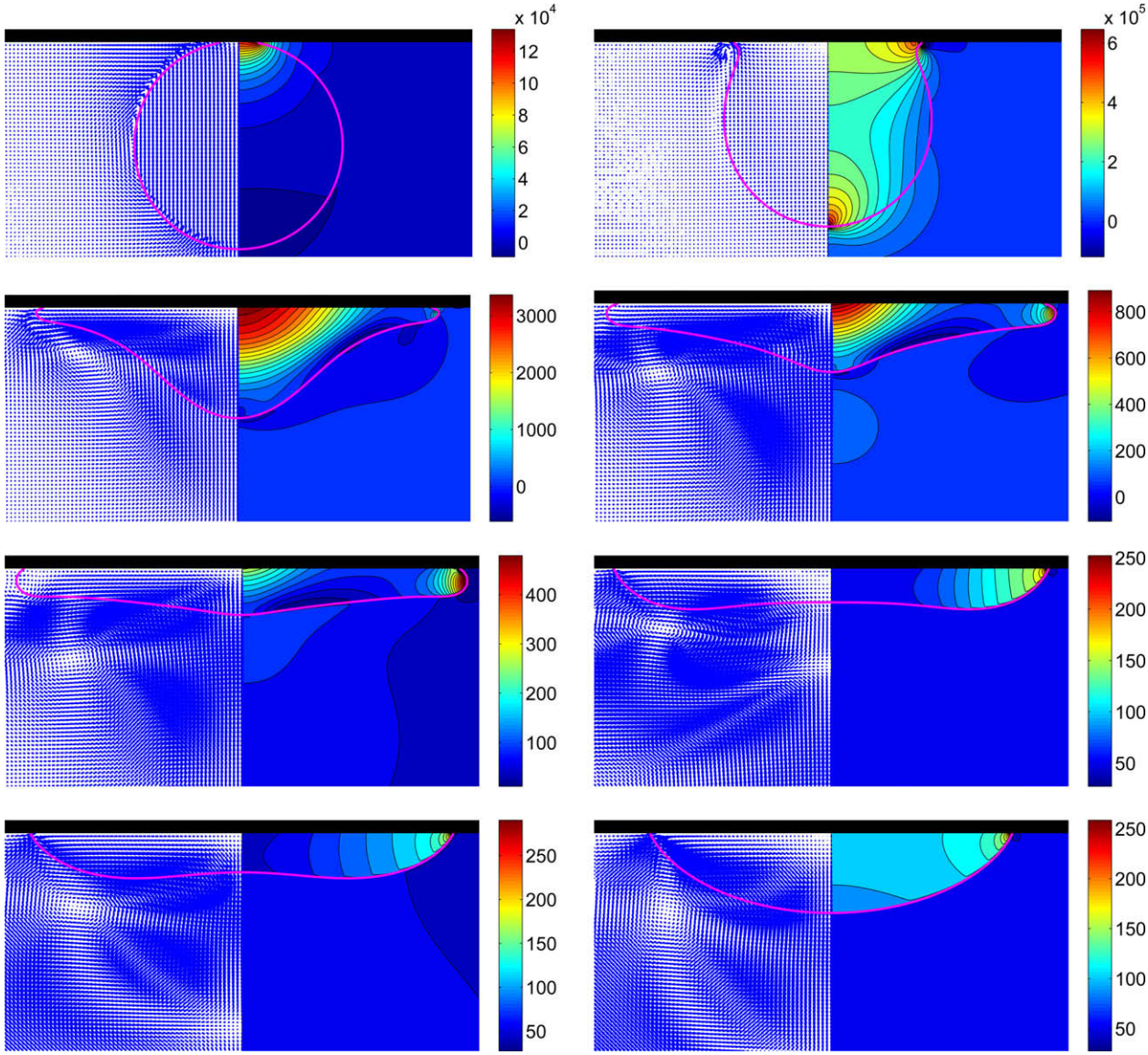

Fig. 4. Evolution of glycerin droplet (Case 1 in Table 1) after impacting on the wax surface. The velocity vectors are plotted on the left and the constant pressure contours on the right. Time evolves from left to right and from top to bottom, and the snapshots are taken at times $t^* = 0.000016, 0.00134, 0.00835, 0.0167, 0.025, 0.1, 0.167$ and 1 ($We = 802$, $Re = 106$, $Eo = 0.285$, Grid: 512×512, $Ca_{\max} = 0.15$, $h_{th} = 2\Delta x$).

advancing phase. Note that the difference between the present results and the experimental data is partly attributed to the relatively coarse (384×384) grid used in the simulations and it can be expected that a finer grid improves the agreement as can be seen in Fig. 9. We next present computational results for Cases 4–6, i.e., a glycerin droplet spreading on a glass substrate (Table 1). For these cases, the static contact angle is set to $\theta_e = 15^\circ$. As can be seen in Fig. 8a the spread factors are initially underpredicted and are then overpredicted in all three cases. However the computational results are overall in a good agreement with the experimental data for all three cases. The contact angles are also reasonably well predicted for these cases as can be seen in Fig. 8b.

Simulations are then performed for Case 1 droplet using various grid resolutions ranging between 128×128 and 768×768 and the results are plotted in Fig. 9 both for the spread factor and the contact angle. As can be seen in this figure, a 512×512 grid resolution is sufficient to obtain grid independent results for this case. The spatial error is quantified in Fig. 10. This figure confirms the expected second order spatial accuracy of the numerical method. Although not shown here, this grid resolution is also found to be sufficient for a grid convergence in the other cases as well.

Next the effects of the cut-off capillary number, $Ca_{\max}$, are examined. For this purpose, simulations are performed for Cases 1 and 3 for the three different cut-off capillary numbers, e.g., $Ca_{\max} = 0, 0.15$ and 0.3 for which the dynamic contact angle is restricted to be $\theta_D = \theta_e = 93^\circ, 46^\circ \leqslant \theta_D \leqslant 140^\circ$ and $31^\circ \leqslant \theta_D \leqslant 155^\circ$, respectively. The results are plotted in Figs. 11 and 12 for Cases 1 and 3, respectively. These figures indicate that $Ca_{\max} = 0.15$ yields the best agreement with the experimental data. We therefore use this value in all the calculations presented in this paper unless stated otherwise.

Finally the effects of the threshold thickness, h_{th} , are examined. The threshold thickness must depend on the grid size in order to satisfy consistency conditions as grid size approaches zero. Computations are performed for Case 1 for various values of the threshold thickness ranging between $h_{th} = \Delta x$ and $h_{th} = 4\Delta x$, and the results are plotted in Fig. 13. It is clear that the results are not very sensitive when $h_{th} \geqslant 2\Delta x$ and the best agreement with the experimental data is obtained for $h_{th} = 2\Delta x$.

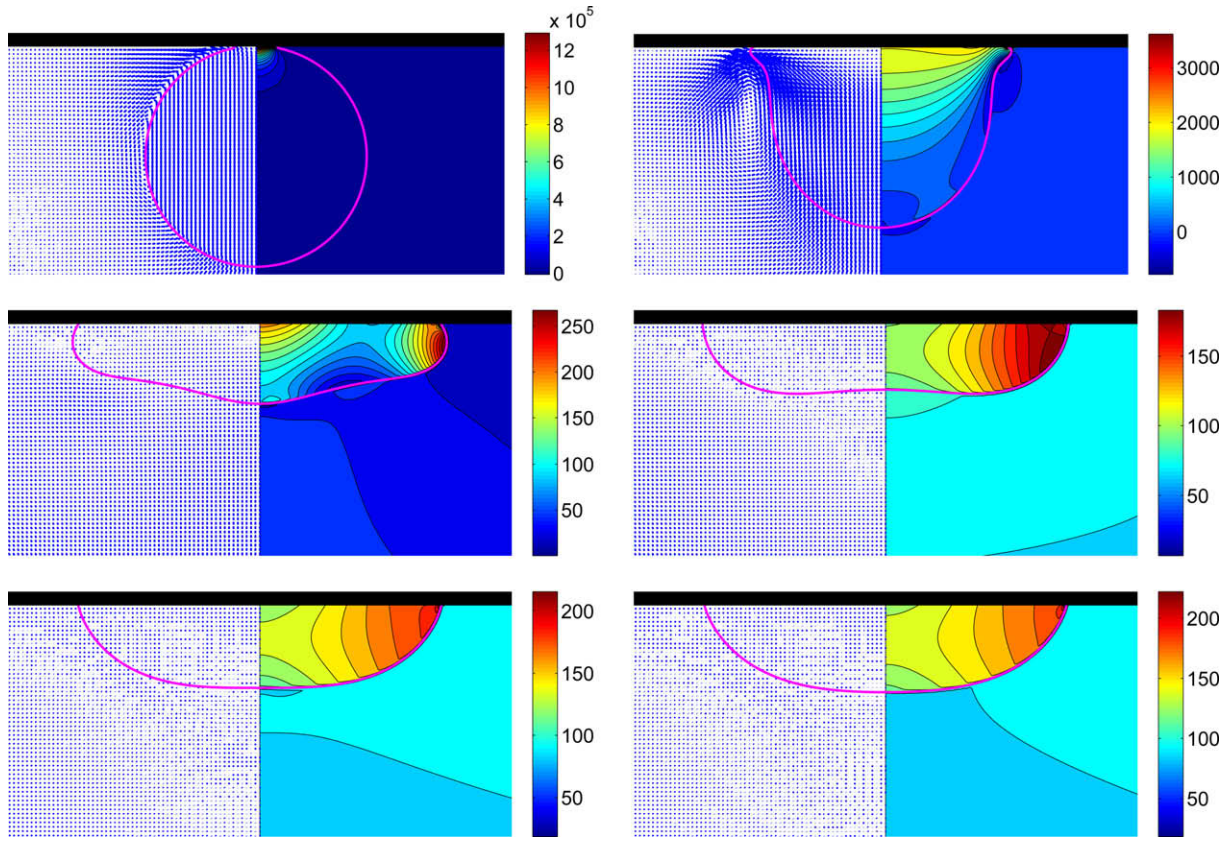

Fig. 5. Evolution of glycerin droplet (Case 2 in Table 1) after impacting on the wax surface. The velocity vectors are plotted on the left and the constant pressure contours on the right. Time evolves from left to right and from top to bottom, and the snapshots are taken at times $t^* = 0.00285, 0.230, 1.439, 2.877, 4.028$ and 4.316 ($We = 93$, $Re = 36$, $Eo = 0.285$, Grid: 512×512, $Ca_{\max} = 0.15$, $h_{th} = 2\Delta x$).

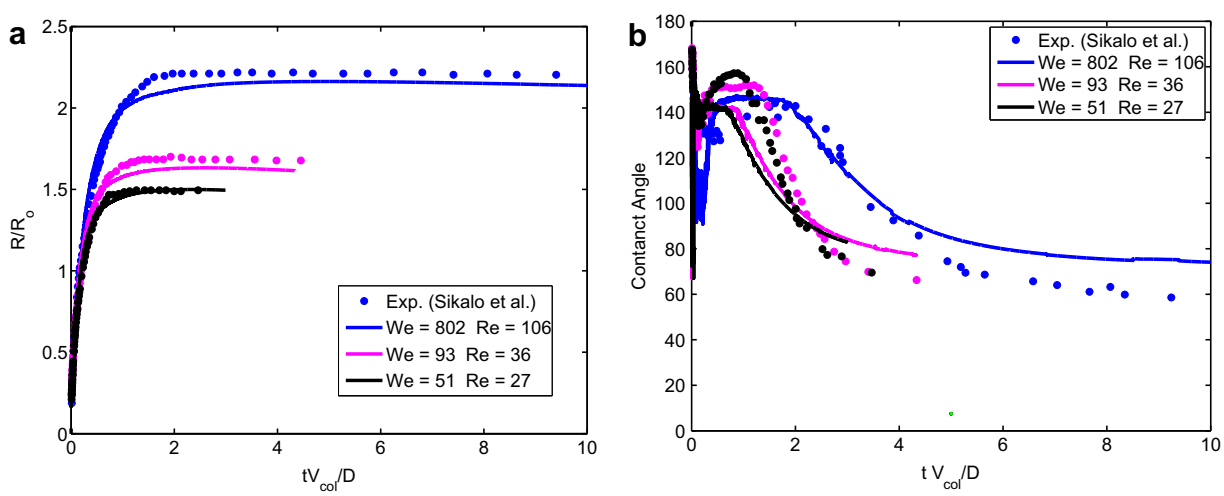

Fig. 6. Glycerin droplet spreading on the wax substrate. Time evolution of (a) the spread factor and (b) the dynamic contact angle ($\theta_e = 93^\circ$, Grid: 512×512, $Ca_{\max} = 0.15$, $h_{th} = 2\Delta x$).

4.3. Effects of non-dimensional numbers

After validating the method against the experimental data, we now study the effects of the non-dimensional numbers on the drop impact and spreading. For this purpose, the effects of the parameters such as equilibrium contact angle, Reynolds and Weber numbers are examined by varying one parameter while keeping the others constant. First Case 1 is selected as the base case and computations are performed for a wide range of equilibrium contact angles varying between 60° and 160° and the results are plotted in Fig. 14. The equilibrium contact angle seems to have little influence on the spread factor in the initial stage where inertial effects are dominant but it has a significant influence both on the spread factor and dynamic contact angle in the later stages. This is an expected result since the droplet should eventually relax to the final equilibrium conditions that are solely determined by the static contact angle (assuming that gravity is negligible). We then select Case 3 as the base case and examine the effects of

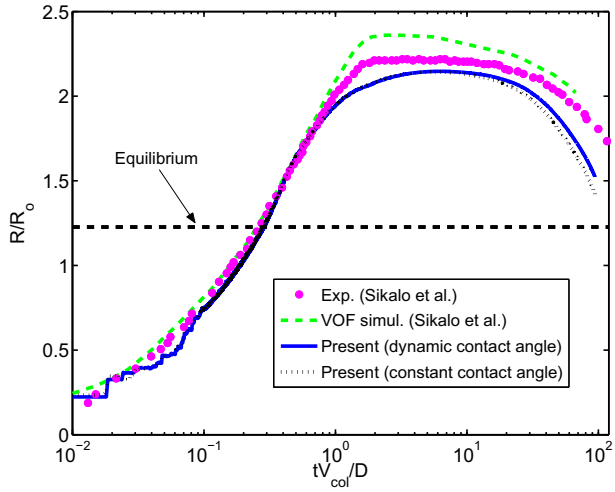

Fig. 7. Effects of dynamic contact angle. Computations are performed using constant (static) and dynamic contact angles and the results are compared with the experimental data and VOF simulation of Sikalo et al. (2005) ($\theta_e = 93^\circ$, Grid: 384×384, $Ca_{\max} = 0.15$, $h_{th} = 2\Delta x$).

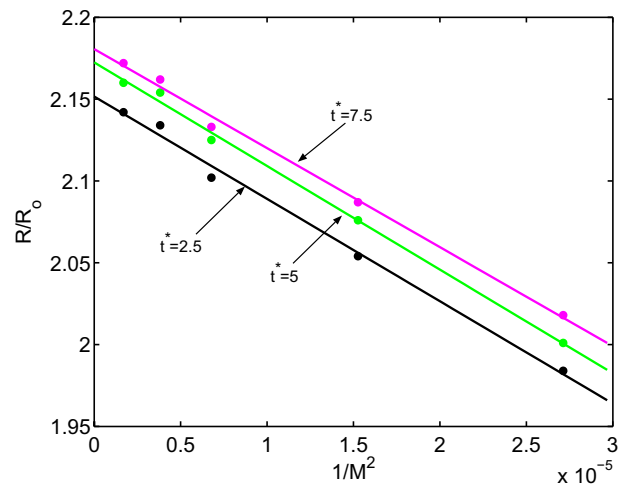

Fig. 10. Grid convergence. The spreading rate against M^{-2} (M is the total number of grid points in radial direction) at $t^* = 2.5, 5.0$ and 7.5 for Case 1 in Table 1. The computations are performed using various grid resolutions ranging between 192×192 and 768×768 ($Re = 106$, $We = 802$ and $\theta_e = 93^\circ$).

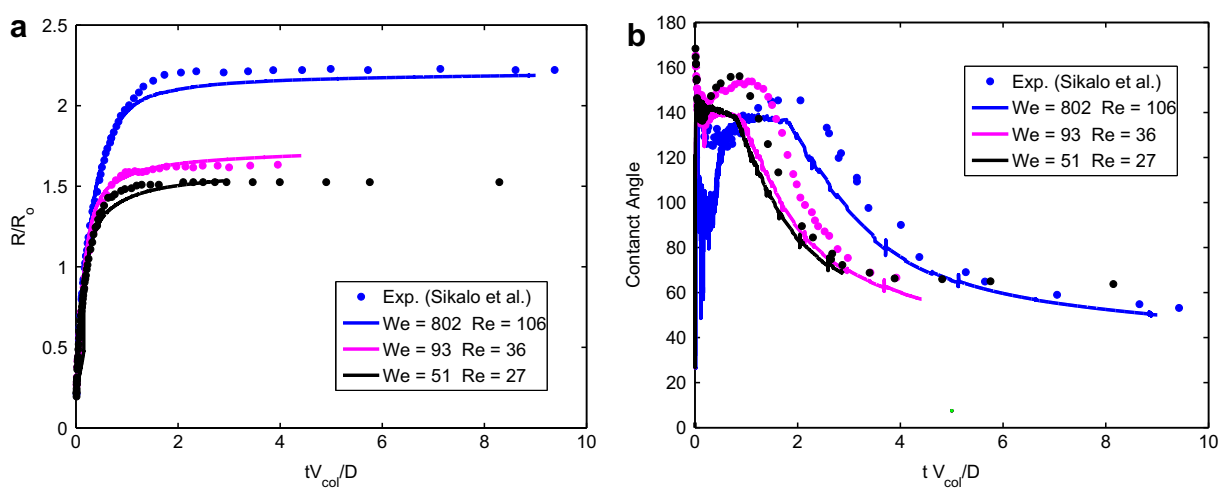

Fig. 8. Glycerin droplet spreading on the glass substrate. Time evolution of (a) the spread factor and (b) the dynamic contact angle ($\theta_e = 15^\circ$, Grid: 512×512, $Ca_{\max} = 0.15$, $h_{th} = 2\Delta x$).

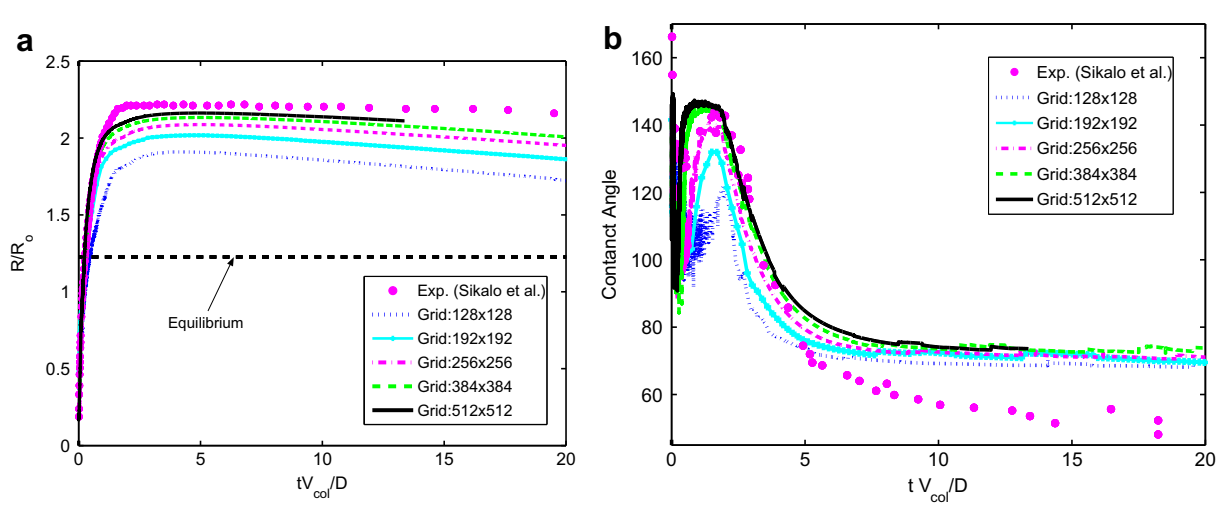

Fig. 9. Grid convergence. (a) Spread factor and (b) contact angle computed using various grid resolutions ranging between 128×128 and 512×512 for Case 1 in Table 1 ($Re = 106$, $We = 802$ and $\theta_e = 93^\circ$).

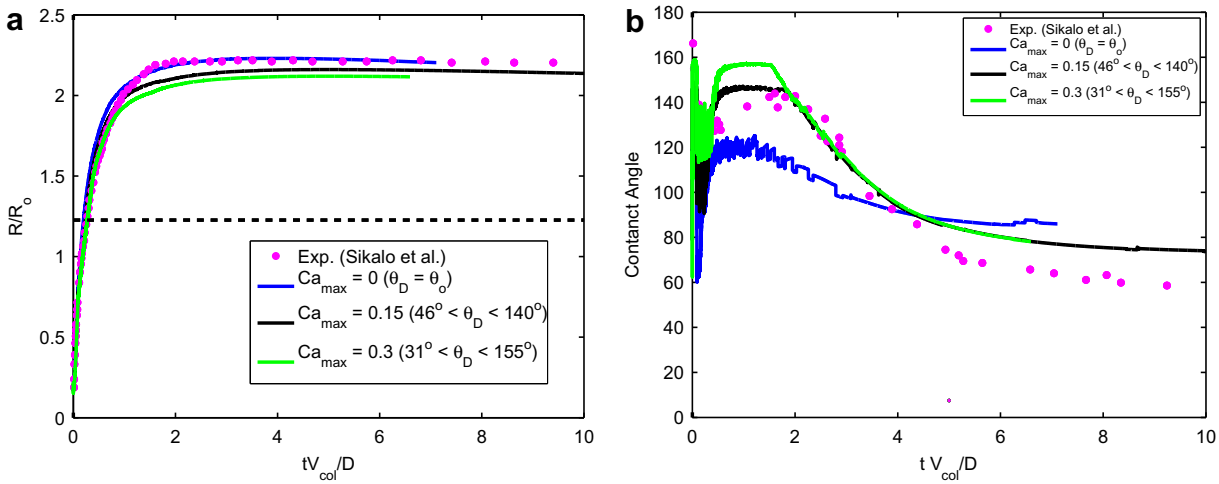

Fig. 11. Effects of the cut-off capillary number, Ca_{max}, for Case 1 in Table 1 (Re = 106, We = 802, Eo = 0.285 and $\theta_D = 93^\circ$).

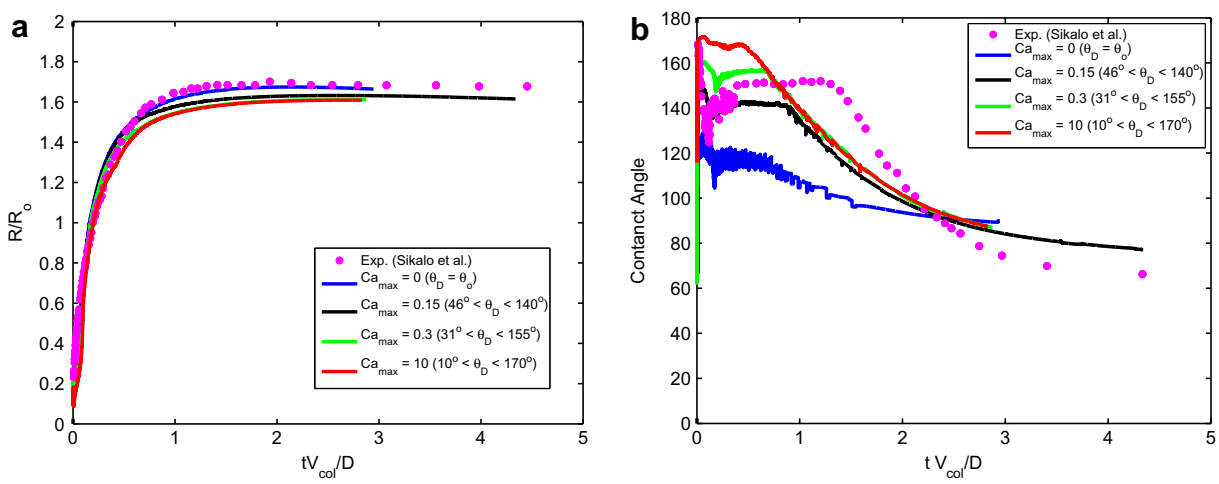

Fig. 12. Effects of the cut-off capillary number, Ca_{max}, for Case 3 in Table 1 (Re = 27, We = 51, Eo = 0.285 and $\theta_e = 93^\circ$).

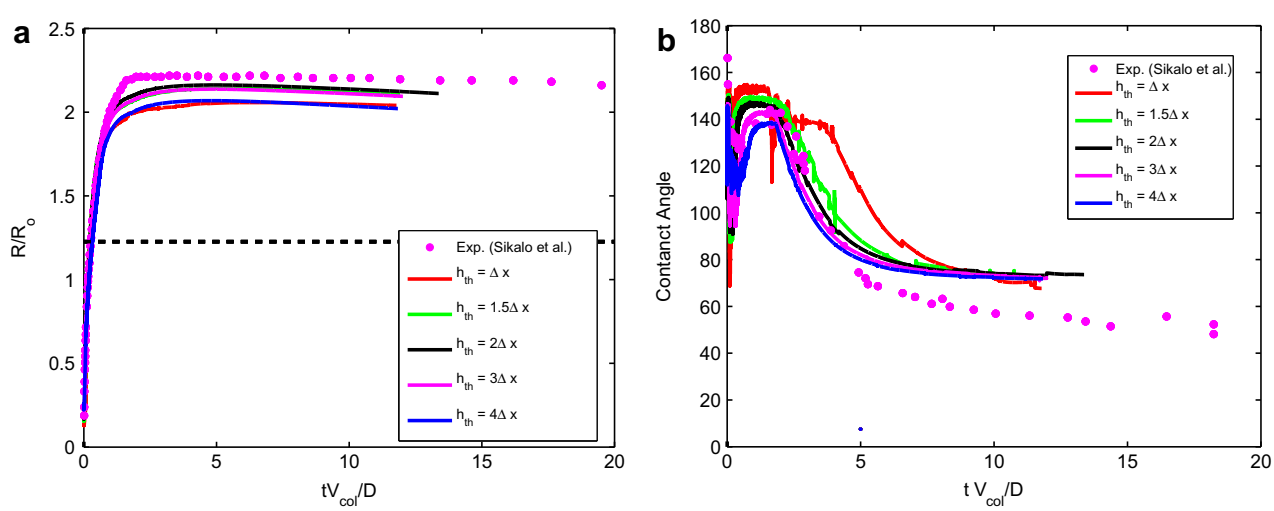

Fig. 13. Effects of the threshold thickness, h_{th}, for Case 1 in Table 1 (Re = 106, We = 802, Eo = 0.285 and $\theta_e = 93^\circ$).

Weber number on the drop impact and spreading by varying the Weber number between 10 and 1080 while keeping the other parameters the same as those in Case 3. The results are plotted in Fig. 15 for the spread factor and dynamic contact angle. The first observation is that the maximum spread increases with increasing Weber number. The second observation is that the droplet reaches

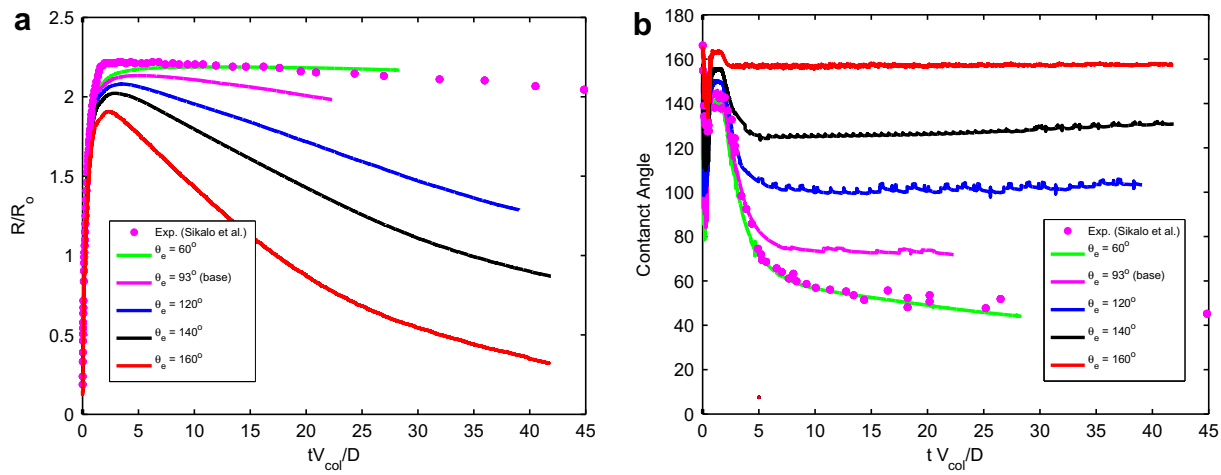

Fig. 14. Effects of the equilibrium contact angle on droplet impact and spreading. Equilibrium contact angle θ_e ranges between 60° and 160° ($Re = 106$, $We = 802$ and $Eo = 0.285$).

equilibrium conditions faster as Weber number decreases. Finally the effects of Reynolds number are shown in Fig. 16 where the spread factor and dynamic contact angle are plotted as a function of non-dimensional time for various Reynolds numbers ranging between $Re = 20$ and 80. It is observed that maximum spread rate increases as Reynolds number increases until about $Re = 60$ but further increase in the Reynolds number does not affect the spreading significantly.

5. Conclusions

A finite-difference/front-tracking method is developed for computational modeling of impact and spreading of viscous droplets on a dry and smooth solid substrates. The method is general and can treat non-wetting, partially wetting and fully wetting cases. The contact angle is specified dynamically using the empirical correlations given by Kistler [13]. The contact angle and the interfacial force are imposed explicitly as boundary conditions at the contact lines. The inertial effects that are dominant especially during the early stages of the droplet impact are accounted for through definition of the threshold distance. Since Kistler's correlation is valid only for small capillary numbers, a cut-off is used to avoid having too large or too small contact angles.

The method is implemented for axisymmetric problems but it is straightforward to extend it to simulate three dimensional flows. The method is first tested for the impact and relaxation of a droplet from the initial spherical shape to its final equilibrium conditions for a wide range of Eotvos numbers. It is found that the computational results are in a good agreements with the analytical solutions for the limiting cases of $Eo \ll 1$ (negligible gravitational effects) and $Eo \gg 1$ (dominant gravitational effects), and there is a transition between a spherical cap and a puddle shape for the intermediate values of Eotvos numbers. The method is then applied to impact and spreading of glycerin droplet on a wax and glass substrates and, the results are compared with the experimental data of Sikalo et al. [20]. It is found that the computational results are in a good agreement with the experimental data. The grid convergence of the method is demonstrated and the effects of numerical parameters such as threshold distance and cut-off capillary number are examined. It is found that the threshold distance has little influence on the computational results as long as it is equal or larger than two Eulerian grid size and the optimal value of the cut-off capillary number is about $Ca_{\max} = 0.15$. After validating the numerical method, further computations are performed to examine the effects of non-dimensional numbers on the drop impact and spreading. It is found that the equilibrium contact angle

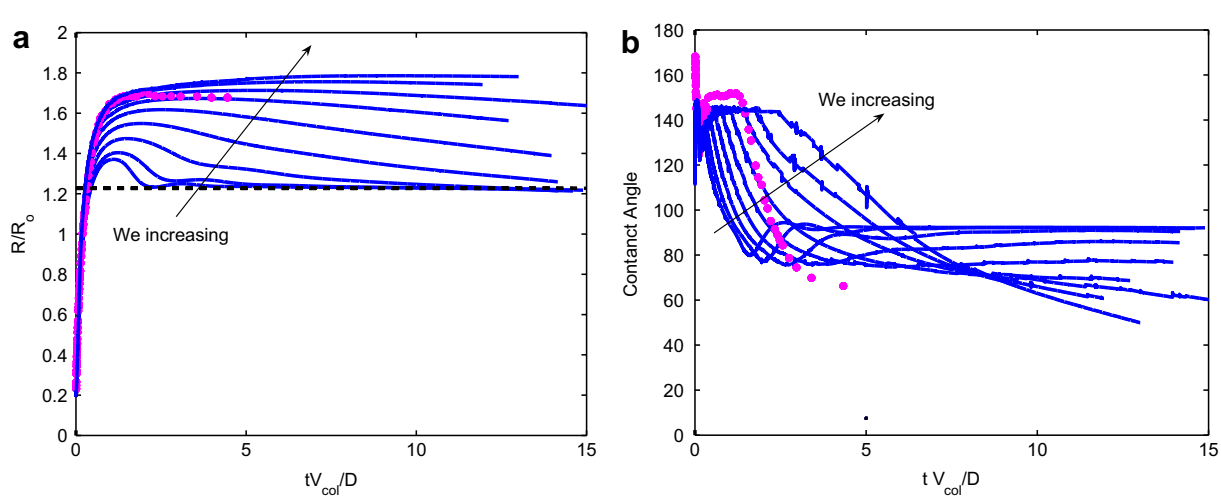

Fig. 15. Effects of Weber number. Weber number varies in the range $We = 10$ and $We = 1080$ ($Re = 27$, $Eo = 0.285$ and $\theta_e = 93°$).

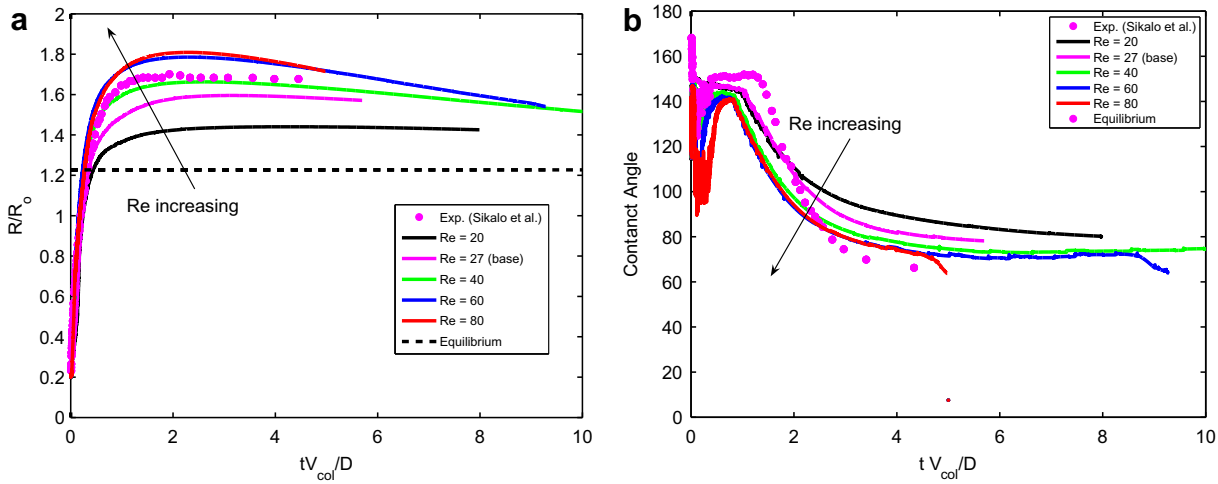

Fig. 16. Effects of Reynolds number. reynolds number varies in the range $Re = 20$ and $Re = 80$ ($We = 51$, $Eo = 0.285$ and $\theta_e = 93^\circ$).

does not have significant influence in the early stages of the drop impact and spreading since the droplet dynamic is essentially determined by the inertial effects during this period. However, the equilibrium contact angle has dominant effect during the later stages. The maximum spreading and time to reach equilibrium conditions are found to be influenced significantly by Weber number, i.e., both the maximum spreading and time to reach the equilibrium conditions increase as the Weber number increases. Finally the effects of the Reynolds number are also examined and it is found that the maximum spreading increases as the Reynolds number increases until about $Re = 60$ but further increase in the Reynolds number does not affect the spreading significantly.

Acknowledgments

We thank the Scientific and Technical Research Council of Turkey (TUBITAK) and Turkish Academy of Sciences (TUBA) for supporting this research through Grant 108M238 and GEBIP program, respectively.

References

[1] Adams J. MUDPACK: multigrid FORTRAN software for the efficient solution of linear elliptic partial differential equations. Appl. Math. Comput. 1989;34:113.
[2] Attinger D, Poulikakos D. Melting and resolidification of a substrate caused by molten microdroplet impact. Trans. ASME: J. Heat Trans. 2001;123:1110–22.
[3] Bussmann M, Mostaghimi J, Chandra S. On a three-dimensional volume tracking model of droplet impact. Phys. Fluids 1999;11:1406–17.
[4] Bussmann M, Mostaghimi J, Chandra S. Modeling the splash of a droplet impacting a solid surface. Phys. Fluids 2000;12:3121.
[5] Chen Y, Mertz R, Kulenovic R. Numerical simulation of bubble formation on orifice plates with a moving contact line. Int. J. Multiphase Flow 2009;35:66–77.
[6] Chorin AR. Numerical solution of the Navier–Stokes equations. Math. Comput. 1968;22:745.
[7] Ding H, Spelt PDM. Inertial effects in droplet spreading: a comparison between diffuse-interface and level-set simulations. J. Fluid Mech. 2007;576:287–96.
[8] Demirci U, Montesano G. Single cell epitaxy by acoustic picoliter droplets. Lab Chip 2007;7:1139–45.
[9] Dussan VEB, Davis SH. On the motion of a fluid–fluid interface along a surface. J. Fluid Mech. 1974;65:71–95.
[10] Francois M, Shyy W. Computation of drop dynamics with the immersed boundary method, part 2: drop impact and heat transfer. Numer. Heat Trans. B 2003;44(2):119–43.
[11] Fukai J, Shiiba Y, Yamamoto T, Miyatake O, Poulikakos D, Megaridis CM, et al. Wetting effects on the spreading of a liquid droplet colliding with a flat surface: experiment and modeling. Phys. Fluids 1995;7:236.
[12] Khatavkar VV, Anderson PD, Duinveld PC, Meijer HEH. Diffuse-interface modeling of droplet impact. J. Fluid Mech. 2007;581:97–127.
[13] Kistler SF. Hydrodynamics of wetting. In: Berg JC, editor. Wettability. New York: Marcel Dekker; 1993.
[14] Mukherjee S, Abraham J. Investigations of drop impact on dry walls with a lattice-Bolzmann model. J. Colloid Interface Sci. 2007;312:341–54.
[15] Muradoglu M, Tryggvason G. A front-tracking method for computation of interfacial flows with soluble surfactants. J. Comput. Phys. 2008;227(4): 2238–62.
[16] Pasandideh-Fard M, Qiao YM, Chandra S, Mostaghimi J. Capillary effects during droplet impact on a solid surface. Phys. Fluids 1996;8:650.
[17] Pasandideh-Fard M, Qiao YM, Chandra S, Mostaghimi J. On a three-dimensional model of droplet impact and solidification. Int. J. Heat Mass Trans. 2002;45:2229–42.
[18] Peskin C. Numerical analysis of blood flow in the heart. J. Comput. Phys. 1977;25:20.
[19] Renardy M, Renardy Y, Li J. Numerical simulation of moving contact line problem using a volume-of-fluid method. J. Comput. Phys. 2001;171:243–63.
[20] Sikalo S, Wilhelm HD, Roisman IV, Jakirlic S, Tropea C. Dynamic contact angle of spreading droplets: experiments and simulations. Phys. Fluids 2005;17:062103.
[21] Shikhmurzaev YD. The moving contact line on a smooth solid surface. Int. J. Multiphase Flow 1993;19:589.
[22] Shikhmurzaev YD. Dynamic contact angles in gas–liquid–solid systems and flow in vicinity of moving contact line. AIChE J. 1996;42:601.
[23] Shikhmurzaev YD. Moving contact lines in liquid–liquid–solid systems. J. Fluid Mech. 1997;334:211–49.
[24] Spelt PDM. A level-set approach for simulations of flows with multiple moving contact lines with hysteresis. J. Comput. Phys. 2005;207:389–404.
[25] Tryggvason G, Bunner B, Esmaeeli A, Juric D, Al-Rawahi N, Tauber W, et al. A front-tracking method for the computations of multiphase flow. J. Comput. Phys. 2001;169:708.
[26] Unverdi SO, Tryggvason G. A front-tracking method for viscous incompressible multiphase flows. J. Comput. Phys. 1992;100:25.
[27] Yarin AL. Drop impact dynamics: splashing, spreading, receding, bouncing. Annu. Rev. Fluid Mech. 2006;38:159–92.
[28] Yu J-D, Sakai S, Sethian J. A coupled quadrilateral grid level set projection method applied to ink jet simulation. J. Comput. Phys. 2005;206:227–51.
[29] Zhao Z, Poulikakos D, Fukai J. Heat transfer and fluid dynamics during the collision of a liquid droplet on a substrate—I. Modeling. Int. J. Heat Mass Trans. 1996;39:2771–89.